Positive resolution of the wound-healing response in lens epithelial cells by $Ti_3C_2T_x$ MXene coatings for use in accommodative intraocular lens devices

To cite this article: Grace Cooksley *et al* 2023 *2D Mater.* **10** 014003

2D Materials

PAPER

Positive resolution of the wound-healing response in lens epithelial cells by $Ti_3C_2T_x$ MXene coatings for use in accommodative intraocular lens devices

Grace Cooksley[1,2,3,*], Marcus K Dymond[1], Nicolas A Stewart[1], Giselda Bucca[1,2], Andrew Hesketh[1,2], Joseph Lacey[3], Yury Gogotsi[4] and Susan Sandeman[1,2,*]

[1] Centre for Stress and Age-Related Disease, University of Brighton, Brighton BN2 4GJ, United Kingdom
[2] Centre for Regenerative Medicine, University of Brighton, Brighton BN2 4GJ, United Kingdom
[3] The Ridley Innovation Centre, Rayner Intraocular Lenses Limited, Worthing BN14 8AG, United Kingdom
[4] A.J. Drexel Nanomaterials Institute and Department of Materials Science and Engineering, Drexel University, Philadelphia, PA 19104, United States of America
* Authors to whom any correspondence should be addressed.

E-mail: g.cooksley@brighton.ac.uk and s.sandeman@brighton.ac.uk

Keywords: titanium carbide, MXene, posterior capsule opacification, intraocular lenses, inflammation, wound-healing response

Supplementary material for this article is available online

OPEN ACCESS

RECEIVED
2 August 2022

REVISED
16 September 2022

ACCEPTED FOR PUBLICATION
28 September 2022

PUBLISHED
19 October 2022

Abstract

Cataract surgery removes the diseased lens of the eye replacing it with an intraocular lens, restoring visual acuity. However, accommodation, the lens' ability to provide dynamic change in focus, is lost. A number of accommodative intraocular lens (AIOL) designs have been considered although none have provided a truly effective clinical AIOL. Two-dimensional titanium carbide ($Ti_3C_2T_x$) MXene has been used as a transparent conductive electrode within an AIOL feasibility study. Nevertheless, the potential for $Ti_3C_2T_x$ to repress excessive inflammation and promote wound healing following cataract surgery has not been considered. Cataract surgery can trigger chronic inflammation and epithelial-mesenchymal transition (EMT) in residual lens epithelial cells (LECs), producing a fibrotic mass across the posterior capsule known as posterior capsule opacification (PCO). With a large surface area and capacity for surface functionalisation, MXene has properties enabling a dual purpose AIOL design with an additional therapeutic role in the repression of pathways leading to PCO development. In this study, $Ti_3C_2T_x$ MXene was investigated to determine its impact on pathways leading to chronic inflammation and EMT using an *in vitro* LECs model. $Ti_3C_2T_x$ MXene was synthesised and characterised using UV-vis spectroscopy, dynamic light scattering and scanning electron microscopy. Changes in markers linked to inflammation and EMT in $Ti_3C_2T_x$-treated LECs were measured using enzyme linked immunosorbent assays, quantitative polymerase chain reaction, scratch assay, RNA sequencing for whole-cell gene expression profiling and lipidomics analysis. $Ti_3C_2T_x$ significantly reduced the expression of pro-inflammatory cytokines by interleukin 1 beta primed LECs and did not advocate EMT, promoting a positive resolution of the wound healing response. This study supports the role of $Ti_3C_2T_x$ within an AIOL design with the potential to repress key developmental pathways leading to PCO.

1. Introduction

Cataracts are the leading cause of preventable blindness globally, characteristically affecting the elderly population [1]. The condition develops as an opacification of the lens due to a loss in chaperone binding and misaligned lens fibres across the visual axis leading to a reduction in visual acuity, poor night vision and sensitivity towards light [2]. Cataracts are treated by surgical intervention where the diseased lens is removed using a phacoemulsification technique and replaced by an intraocular lens (IOL) [2]. The implanted IOL restores visual acuity. However, there is reliance on spectacles for adjustable change

in focus otherwise known as accommodation [3]. Current accommodative IOL (AIOL) designs are yet to provide true accommodation without negating visual outcome [4]. The requirement for an innovative AIOL design has expanded into the field of two-dimensional (2D) nanomaterials, specifically the family of transition metals carbides or nitrides known as MXenes [5].

MXenes, a class of 2D nanomaterials, were discovered by researchers at Drexel University in 2011 [6]. M stands for an early transition metal and X for carbon or nitrogen, forming 2D carbide or nitride layers. The surface of MXene layers is terminated by O, OH, F or other functional groups (T_x) coming from the etching solution used to produce MXenes by selective etching. Surface terminations make MXene hydrophilic and dispersible in water [7]. The unique and favourable properties of MXenes have been exploited for biomedical use including in the development of antimicrobial agents, photothermal treatments and diagnostic biosensing [8–10]. More recently, $Ti_3C_2T_x$ (MXene) has been applied as a transparent conductive electrode (TCE) in smart ocular devices due to its advantageous properties of transparency, flexibility and conductivity [5]. Yin *et al* [11], synthesised amorphous germanium sulphide films with $Ti_3C_2T_x$ as a TCE contact for broadband photodetectors. Moreover, Ward *et al* [5], demonstrated a proof-of-concept test cell that utilised a formulation of liquid crystals and $Ti_3C_2T_x$ to provide an adjustable focal lens in an AIOL feasibility study. Despite the various applications of MXene within biomedicine, its biocompatibility is poorly understood. To date, MXene has been investigated for cell toxicity, reactive oxygen species generation and upregulation of pro-inflammatory markers [5, 12]. Nevertheless, the impact of MXene on ocular physiology, inflammatory upregulation and the wound healing response for ophthalmic medical device applications has yet to be investigated.

Posterior capsule opacification (PCO) is a common complication arising from cataract surgery [13]. Patients have a 5%–50% risk of developing PCO two to five years post-surgery [14]. PCO manifests as an agglomeration of fibrotic cells and extracellular matrix (ECM) across the visual axis and can be referred to as a secondary cataract due to the similarity in appearance and symptoms of a cataract [15, 16]. PCO is thought to be incited by a wound healing response in residual lens epithelial cells (LECs) within the capsular bag, the membrane where the lens is situated, triggered by surgically induced trauma [17]. Long-term elevated levels of pro-inflammatory cytokines interleukin (IL)-1β and IL-6 contribute to monocyte migration and activation of transforming growth factor beta 2 (TGF-β2), promoting the epithelial-mesenchymal transition (EMT) of residual LECs [18–20]. These transformed myofibroblasts migrate across the visual axis of the implanted IOL, causing a visual obstruction. The condition can be treated by neodymium-doped yttrium aluminium garnet laser ablation. However, this treatment can lead to IOL displacement, retinal detachment, mild anterior uveitis and a transient rise in intraocular pressure [21]. Drug-eluting IOL coatings have been explored as an alternative therapeutic intervention to allow direct interaction with residual LECs within the capsular bag to repress an excessive inflammatory response and EMT following invasive cataract surgery [22].

Therapeutic agents have been investigated to prevent PCO development [23]. Despite this, there are no pharmaceutical therapies for patients to prevent or manage PCO [24]. $Ti_3C_2T_x$ has been exploited in drug eluting nanoplatforms as chemotherapeutic agents due to their ability to be processed as ultrathin films, manipulation of surface termination groups and intercalation of organic molecules [8, 10, 25]. It has also been shown that $Ti_3C_2T_x$ has the capacity to repress lipopolysaccharide mediated monocyte expression of inflammatory cytokines indicating an anti-inflammatory rather than pro-inflammatory mechanism of action [12]. Ye *et al* [26], used Ti_3C_2-coated IOLs for combinational photothermal therapy and drug release to prevent LEC migration and suppress the inflammatory response. Whilst $Ti_3C_2T_x$ has been incorporated into an AIOL prototype and demonstrated efficacy in terms of altered lens dioptric power there is little known about the impact of $Ti_3C_2T_x$ on activation of inflammatory and EMT pathways linked to the primary complication associated with IOL implantation, PCO. This study therefore aimed to evaluate the impact of $Ti_3C_2T_x$ coatings on mechanisms leading to excessive inflammatory response, tendency of LECs to undergo myofibroblast differentiation and upregulation of pathways leading to EMT using *in vitro* LECs models. It was hypothesised that $Ti_3C_2T_x$ could act to repress LECs intracellular pathways leading to PCO by inhibiting mechanisms which upregulate the pro-inflammatory response, myofibroblast transdifferentiation and migration. This study presents for the first time, the ability of $Ti_3C_2T_x$ to suppress hyperinflammation and propensity towards EMT of LEC undergoing the wound healing response, contributing to PCO development.

2. Methods

2.1. Synthesis of $Ti_3C_2T_x$ (MXene)

Lithium fluoride (0.8 g) (Sigma Aldrich, UK) was added to 9 M hydrochloric acid (10 ml) (Sigma Aldrich, UK) at 35 °C (IKA RCT Basic Hot Plate Magnetic Stirrer Stirring Digital 115V). Ti_3AlC_2 (0.5 g) (A.J. Drexel Nanomaterials Institute, Drexel University, USA), was gradually added over 5 min and

constantly stirred for 24 h. The solution was washed with deionised (DI) water and repeated centrifugation for 5 min at 3500 rpm until the colloidal solution reached a pH of 5–6 (T515 rotor, ALC PK 120R Centrifuge). The sediment was resuspended and shaken for 15 min at speed 6, 50 Hz (Flask Shaker, Gallenkamp, Germany) then centrifuged for 1 h at 3500 rpm. The colloidal solution was ice-bath sonicated for 20 min then centrifuged for an additional hour (Elmasonic S30H Ultrasonic Cleaner, Germany). The delaminated product was decanted and a set volume was vacuum filtered and weighed to calculate the concentration (mg ml^{-1}). Solutions were stored at −20 °C prior to use.

2.2. Physical characterisation of $Ti_3C_2T_x$ (MXene)

Particle size analysis was conducted using dynamic light scattering (DLS) (Zetasizer Nano ZS, Malvern Panalytical, UK). Scanning electron microscopy (SEM) was performed at Drexel University (Zeiss Supra 50VP, Germany). Ultraviolet-visible (UV-vis) spectroscopy was carried out in the wavelength range of 200–1000 nm to confirm the synthesis of $Ti_3C_2T_x$ (UV-2401PC, Shimadzu Corporation, Japan).

2.3. Contact angle analysis

$Ti_3C_2T_x$ was spin-coated onto RayONE hydrophobic IOLs (RAO800C; Rayner Intraocular Lenses, Ltd. UK) by first pre-treating the optic with atmospheric plasma etching for 3 min at 11 sccm, 10 cm^3 min (Henniker Plasma, UK) then spin-coating 30 μl of 3 mg ml^{-1} $Ti_3C_2T_x$ suspension three times using an Ossila Spin Coater (Ossila, UK) in a two-step method of 5000 rpm for 30 s then 6000 rpm for 30 s. $Ti_3C_2T_x$-coated hydrophobic lenses were compared to uncoated hydrophobic and hydrophilic IOL (RAO600C; Rayner Intraocular Lenses, Ltd. UK). Contact angle measurements were taken using SCA 20 software, OCA 15EC (DataPhysics Instruments GmbH, Germany). The sessile drop method was used with a dosage of 5 μl DI water.

2.4. Spray-coating of $Ti_3C_2T_x$ (MXene)

Twelve-well tissue culture plates were covered in parafilm to isolate the coating areas and clamped into place, at a set distance of 15 cm away from the spray nozzle. A set volume, calculated by the stock concentration was applied in a left to right motion using an Airbrush Compressor TC-20 and Master Airbrush (Model G22, TCP Global, USA). Constant heat was applied by an external source to achieve uniform drying between coats. $Ti_3C_2T_x$-coated wells were sterilised by UV light for 1 h prior to use in cell studies.

2.5. Characterisation of $Ti_3C_2T_x$ (MXene) coatings

$Ti_3C_2T_x$ coatings were characterised by SEM imaging. A 12-well tissue culture plate was spray-coated with 5 mg ml^{-1} $Ti_3C_2T_x$ as described in 2.4. The plate was fragmented into smaller sections and mounted to the side of a hexagonal nut, perpendicular to the electron beam. High-resolution images were produced through SEM (Field Emission Scanning Electron Microscope, Zeiss Sigma, Germany), with a 1.5 kV accelerating voltage. The $Ti_3C_2T_x$ coating thickness was determined by measuring the $Ti_3C_2T_x$ layer, where the tissue culture plate was used as the baseline. The stability of the coatings was measured by incubating Minimum Essential Medium (MEM) with 5 mg ml^{-1} $Ti_3C_2T_x$ coatings at 37 °C, 5% CO_2 for 24 h as per experimental conditions. The culture media was analysed pre- and post- $Ti_3C_2T_x$ coatings incubation using UV–vis spectroscopy, as detailed in 2.2.

2.6. Cell culture of human LEC lines HLE-B3 and FHL124

The human LEC line HLE-B3 (American Type Culture Collection ATCC CRL-11421) was cultured in MEM supplemented with 10% foetal bovine serum (FBS) and 1% non-essential amino acids. Foetal human lens (FHL124) cells were kindly gifted from Professor Michael Wormstone (University of East Anglia), characterised in Wormstone *et al* [27]. FHL124 cells were cultured in MEM supplemented with 5% FBS. Both cell types were passaged by standard trypsinisation. The cells were washed in phosphate buffer saline (PBS), incubated in 2 ml of Trypsin (Gibco, UK) for 2 min, followed by addition of the equivalent of two volumes of trypsin neutralising MEM. The cell suspension was collected in a universal tube and centrifuged at 500 rpm for 5 min. The cell pellet was resuspended in 1 ml MEM for quantification of cell concentration using hemocytometry.

2.7. Enzyme immunoassay—interleukin 1 beta (IL-1β) primed cells with $Ti_3C_2T_x$ (MXene) colloidal solution

HLE-B3 cells were seeded into the wells of a 12-well tissue culture plate at a concentration of 1×10^5 cells ml^{-1} and primed with 50 ng ml^{-1} IL-1β (BD Pharmingen™, UK) for 24 h at 37 °C, 5% CO_2. The media was removed, and the wells were washed in PBS (Thermofisher Scientific, UK) thrice. In the $Ti_3C_2T_x$ treated conditions, 0.5 mg ml^{-1} or 1 mg ml^{-1} of $Ti_3C_2T_x$ colloidal solution was suspended in media and added to the relevant experimental wells whilst the cell only controls were incubated with media alone. Samples were taken 24 h post-treatment and stored at −20 °C. Technical and experimental repeats were carried out in triplicate. IL-8 and IL-6 in undiluted cell conditioned samples were quantified using Human IL-8 and IL-6 BDOptEIA enzyme-linked immunosorbent (ELISA) assays according to manufacturer's instructions (BD Biosciences, UK).

Table 1. Primers for genes of interest (Qiagen, UK).

Gene Name	Protein Encoded	Catalog Number
ACTB_2	Actin	QT01680476
CXCL1	C-X-C motif chemokine ligand 1	QT00199752
IL-6	Interleukin-6	QT00083720
IL-1β	Interleukin-1 beta	QT00021385

2.8. Enzyme immunoassay—IL-1β primed cells with $Ti_3C_2T_x$ (MXene) coatings

HLE-B3 cells were seeded into the wells of a 12-well tissue culture plate at a concentration of 1×10^5 cells ml^{-1} and primed with 100 ng ml^{-1} IL-1β (BD Pharmingen™) for 24 h at 37 °C, 5% CO_2. In the $Ti_3C_2T_x$ treated conditions, wells were spray-coated with 5 mg ml^{-1} coatings as described in 2.4. Treatment groups included $Ti_3C_2T_x$-treated cells (5 mg ml^{-1} coatings), IL-1β-treated cells (100 ng ml^{-1}) and cells treated with $Ti_3C_2T_x$ and IL-1β. Cell only and media only controls were also included. Samples were taken 24 h post-treatment and stored at −20 °C. Technical and experimental repeats were carried out in triplicate. IL-1β and IL-6 in cell conditioned samples was quantified using Human IL-8 and IL-6 BDOptEIA ELISA assays according to manufacturer's instructions (BD Biosciences, UK). Samples were analysed neat, except the IL-1β-treated cell condition which was analysed using a dilution factor of 1 in 50.

2.9. Quantitative polymerase chain reaction (q-PCR)

HLE-B3 cells were seeded into the wells of a 12 well tissue culture plate at a concentration of 6×10^5 cells ml^{-1}. Treatment and control groups were set up to include cells only, $Ti_3C_2T_x$-treated cells (5 mg ml^{-1} coatings), IL-1β-treated cells (100 ng ml^{-1}) and cells treated with $Ti_3C_2T_x$ and IL-1β. Each treatment and control group were prepared in duplicate and incubated for 24 h at 37 °C, 5% CO_2. At 24 h, cells were trypsinised, and centrifuged at 12 G for 5 min to form a cell pellet. Total ribonucleic acid (RNA) was extracted using a RNeasy® Mini Kit (Qiagen, UK) and quantified using a Nanodrop Lite Spectrophotometer (Thermo Fisher Scientific, UK). g-deoxyribonucleic acid (DNA) elimination and cDNA generation was achieved using a QuantiTect® Reverse Transcription Kit (Qiagen, UK). Gene expression of primers (table 1) was quantified using a Rotor-Gene® SYBR® Green PCR Kit (Qiagen, UK) against the housekeeping gene actin.

2.10. Wound-healing assay

Three wells of a 12 well tissue culture plate was spray coated with $Ti_3C_2T_x$ at a concentration of 2 mg ml^{-1} and sterilised according to the method described in section 2.4. The coated and cell only control wells were seeded with HLE-B3 cells at a concentration of 5×10^5 cells ml^{-1} and were then incubated for 24 h at 37 °C, 5% CO_2. The media was aspirated, and a vertical scratch was made using a p200 tip through the centre of each well. The wells were gently washed thrice in warmed PBS and fresh media was added. Images were captured at 0, 24, 48, 72 and 120 h using a Zeiss Primovert HDcam (Carl Zeiss Microscopy GmbH, Germany). Cells were fixed with 3.7% formaldehyde (Sigma Aldrich, UK) diluted in PBS and stained with 0.1% crystal violet in PBS (Sigma Aldrich, UK) at 0 and 120 h time points. Wound area, scratch width and wound closure rate was quantified using Fiji: Image J analysis [28].

2.11. Immunocytochemistry for cell differentiation markers

FHL124 cells were seeded at a concentration of 1×10^5 cells ml^{-1} onto 16 mm coverslips (Fisherbrand™, UK). Treatment and control groups were set up to include cell only, $Ti_3C_2T_x$-treated cells (2 mg ml^{-1} coatings), TGF-β2-treated cells (20 ng ml^{-1}) and cells treated with $Ti_3C_2T_x$ and TGF-β2 and included a no primary antibody control. Coverslips were incubated for 24 h at 37 °C, 5% CO_2, rinsed in PBS then fixed in 3.7% formaldehyde (Sigma Aldrich, UK) in PBS for 10 min. The coverslips were washed in 10% (v/v) bovine serum albumin (BSA) in PBS (Sigma Aldrich, UK), then in 0.5% (v/v) Triton-X (Tx) in PBS (Sigma Aldrich, UK) for 20 min and finally in 5% (v/v) BSA, 0.5% (v/v) Tx diluted in PBS. Alpha smooth muscle actin (α-SMA) (1 μg ml^{-1}) (Thermofisher Scientific, UK), vimentin (2 μg ml^{-1}) (Thermofisher Scientific, UK), and SMAD2/3 (1:50 dilution) (Cell Signalling Technology, UK) antibodies were added and coverslips were incubated for 24 h at 4 °C. The coverslips were washed in PBS thrice, followed by a 4 h incubation with secondary antibody Goat anti-Mouse IgG (1 μg ml^{-1}) at 4 °C in the dark. Coverslips were washed and 10 μl 4′,6-diamidino-2-phenylindole (DAPI) (1 mg ml^{-1}) was added for 10 min. The coverslips were inverted onto microscope slides and visualised using a Zeiss LSM800 Confocal Microscope (Serial No. 3347002202. Carl Zeiss Microscopy GmBh, Germany). An excitation filter of 488 nm was used. Images were analysed using Fiji: Image J analysis. Fluorescence intensity over area was calculated for cytoskeletal markers vimentin and α-SMA. SMAD2/3 was quantified by cell counting of the stained nuclei [29]. Total cell counts using DAPI nuclei staining was used to normalise SMAD2/3 stain for cell number across the conditions. Any detection of non-specific binding of the secondary antibody in the no primary antibody incubation control was subtracted from the cell only and treated cell conditions.

2.12. Western blot for cell differentiation markers

FHL124 cells were seeded into the wells of a 12 well tissue culture plate at a concentration of

5×10^5 cells ml^{-1}. Treatment and control groups included cells only, $Ti_3C_2T_x$-treated cells (2 mg ml^{-1} coatings), TGF-β2-treated cells (20 ng ml^{-1}) and cells treated with $Ti_3C_2T_x$ and TGF-β2. Plates were incubated for 24 h at 37 °C, 5% CO_2. Cells were trypsinised, centrifuged at 12 G for 5 min, then placed in ice with the addition of 50 μl radioimmunoprecipitation assay (RIPA) buffer and proteinase inhibitor (ThermoFisher Scientific, UK). Samples were centrifuged for 40 min at 4 °C and the supernatant was collected for quantification of total protein using the Bradford assay according to manufacturer's instructions. Samples were diluted with RIPA buffer and 6× Laemmli buffer to 20 μg/25 μl then heated at 95 °C for 5 min. The total volume of the samples was loaded into the wells of a 10% SDS-TrisHCl gel (BioRad, UK) and proteins were separated at a constant voltage of 100 V for 1 h. The proteins were transferred to a polyvinyl difluoride membrane using the Mini Trans-Blot® Cell (BioRad, UK) set at a constant voltage of 100 V for 1 h. The membrane was blocked with 5% BSA in tris-buffered saline with 1% Tween® 20 (TBST) (Sigma Aldrich, UK), then incubated with anti-α-SMA (1:250 dilution) (ThermoFisher Scientific, UK), vimentin (1:500 dilution) (ThermoFisher Scientific, UK) and SMAD2/3 (1:250 dilution) (Cell Signalling Technology, UK) antibodies for 16–18 h at 5 °C. Beta-actin (1:500 dilution) (ThermoFisher Scientific, UK) was included as a housekeeping control. After four 10 min wash cycles in TBST, the membrane was incubated in secondary antibody goat anti-mouse IgG1 (HRP) (1:1000 dilution) (ThermoFisher Scientific, UK) for 1 h at room temperature (RT). The membrane was washed again and developed using Image Studio™ software and a C-Digit Blot Scanner (LI-COR Model no. 3600, LI-COR Inc. Lincoln, NE, USA). Membranes were stripped three times, re-developed to show a clear stripped blot then re-probed.

2.13. RNA sequencing (RNA-Seq)

FHL124 cells were seeded into the wells of a 12 well tissue culture plate at a concentration of 6×10^5 cells ml^{-1}. Treatment and control groups were set up to include cells only, $Ti_3C_2T_x$-treated cells (5 mg ml^{-1} coatings), IL-1β-treated cells (100 ng ml^{-1}) and cells treated with $Ti_3C_2T_x$ and IL-1β. Samples were prepared in triplicate and were incubated for 24 h at 37 °C, 5% CO_2. Cells were trypsinised and centrifuged at 12 G for 5 min. RNA extraction was performed using an miRNeasy Mini Kit (Qiagen, UK). All extracted RNA was quality checked using the RNA screen tapes and the Agilent TapeStation 4200 instrument. All had a RIN^e above 7.9. mRNA purification from 200 ng of total RNA input was performed as per the NEBNext® Poly(A)mRNA Magnetic Isolation Module (New England Biolabs, UK). Library preparation from purified mRNA was performed using the NEBNext® Ultra™ II Directional RNA Library Prep Kit for Illumina® (New England Biolabs, UK) protocol. Libraries were quality checked using the D100 High Sensitivity kit and the TapeStation 4200 instrument. The DNA from each library was quantified using the Qubit v2 fluorometer and all libraries were normalized to 2 nM final concentration before pooling. The library pool was quantified by q-PCR using NEBNext® Library Quant Kit for Illumina® (New England Biolabs, UK) and sequenced on NextSeq 500 sequencer High Output kit 150 cycle 2 × 75 PE.

Approximately 30–40 million sequencing read pairs were obtained per sample. These were subjected to adapter and quality threshold trimming using trimgalore [30, 31] and transcripts in the human genome (GRCh38) were quantified from the trimmed reads using salmon [32]. The transcript count data were summarised to the gene-level and analysed for differential expression using DESeq2 [33]. Gene set enrichment analysis (GSEA) and functional over-representation analysis of lists of significantly differentially expressed genes (FDR $\leqslant$ 0.05) was performed using clusterProfiler [34].

2.14. Bligh-Dyer [35] lipid extractions and sample preparation for mass spectrometry (MS)

Samples were prepared as described in 2.13. Cells were trypsinised, centrifuged at 12 G for 5 min. Pelleted cells were suspended in $NaCl_{(aq)}$ solution (800 μl, 0.9 wt%). SPLASH LipidoMIX internal standard (10 μl, Avanti Polar lipids) was added followed by chloroform (1.0 ml), methanol (2.0 ml), chloroform (1.0 ml) and water (1.0 ml) vortexing between each addition. After centrifugation at 1500 rpm for 10 mins at RT, the organic bottom layer was removed and dried under nitrogen (40 °C). Dry lipid films were re-dissolved in chloroform (*circa* 100 μl) and transferred to high performance liquid chromatography (HPLC) amber vials fitted with glass inserts (2 ml), re-dried under nitrogen (40 °C) and stored at −20 °C, prior to analysis. HPLC grade solvents and water were used throughout.

2.15. Lipidomics analysis by HPLC-MS

Lipid analyses were performed on a hybrid quadrupole Orbitrap mass spectrometer (Q Exactive, ThermoScientific) fitted with an ultra-high-performance LC system (Ultimate 3000, ThermoScientific). Sample separation was achieved using reversed phase chromatography column (ACQUITY UPLC HSS T3 Column, 100 Å, 1.8 μm, 2.1 mm × 100 mm, Waters Corporation) held at 40 °C with the following gradient. Solvent A; (60:40 v/v); water (Hypergrade for LC-MS, LiChrosolv®, Merck-KGaA): acetonitrile (MSsuprasolve®, Sigma Aldrich) and 10 mM ammonium formate (99.995%, Sigma Aldrich) and solvent B; (90:10) isopropanol

(Optima™LC/MS Grade, Fisher Scientific): acetonitrile (MSsuprasolve®, Sigma Aldrich) and 10 mM ammonium formate (99.995%, Sigma Aldrich). Separation was achieved at a flow rate of 200 μl min^{-1}. Flow was diverted to waste for the first 30 s, using 0% B (0–1 min), rising to 100% B in 53 min; 100% B for 3 min, reduced to 0% B in 1 min and equilibrated for 9 min. Samples were stored in the autosampler (4 °C), injecting with μl pick-up injection method (5 μl). Samples were analysed in positive and negative ionisation mode using heated electrospray ionization. Spray voltage (3500 V positive mode, −3500 V negative mode), sheath gas (45 au), auxiliary gas (8 au), sweep gas (1 au) probe temperature (350 °C), capillary temperature (320 °C) and S-Lens (50 °C). MS data were acquired in a data-dependant manner. Full scan profile MS spectra (250–1200 m z^{-1}) were recorded at a resolution of 140 000@200 m z^{-1}, with fragmentation of the top ten most intense precursor ions. Dynamic exclusion was (10 s), charge exclusion (none), automatic gain control (AGC) target (1×10^6 and full scan maximum injection time (50 ms). Precursor ions were fragmented by higher-energy collisional dissociation (HCD) using a normalized stepped collision energy of 25 and 30; default charge state of 1. MS/MS scans were recorded performed at a resolution of 17 500@200 m z^{-1} in profile mode, AGC target value (1×10^5), maximum injection time (100 ms) with an isolation window of 1.0 m z^{-1}.

2.16. Bioinformatic association of HPLC MS/MS features with lipid identities

Thermofisher raw format (.raw) file were converted to mzXML files using MSConvert (Proteowizard) [36]. Lipid identities were assigned using Lipidex software [37], with Lipidex_HCD_Formic, Lipidex_HCD_Hydroxy, Lipidex_HCD_Plants, Lipidex_HCD_ULCFA and Lipidex_Splash_ISTD_Formic spectral libraries. HPLC alignment files were generated using MZMine [38], Thermofisher raw format (.raw) files were imported to MZmine and features were detected using the Mass detection algorithm. Full bioinformatic settings are included in table S1.

2.17. Lipid analysis and quantification

Lipids were quantified relative to isotopic standards. PE, Plasmanyl-PE and Plasmenyl-PE species were quantified to the PE standard 15:0–18:1(d7) PE (5.3 μg ml^{-1}), PC, PC(OH), Plasmanyl-PC and Plasmenyl-PC were quantified to the PC standard 15:0–18:1(d7) PC (150.6 μg ml^{-1}). DG, TAG, PI, PG and SM lipids were quantified to 15:0–18:1(d7) DG (8.8 μg ml^{-1}), 15:0–18:1(d7)-15:0 TAG (52.8 μg ml^{-1}), 15:0–18:1(d7) PI (8.5 μg ml^{-1}), 15:0–18:1(d7) PG (26.7 μg ml^{-1}) and d18:1–18:1(d9) SM (29.6 μg ml^{-1}), respectively. Lyso PE and Lyso PC were quantified relative to 18:1(d7) Lyso PE (4.9 μg ml^{-1}) and 18:1(d7) Lyso PC 23.8 μg ml^{-1}).

2.18. Statistical analysis

Data processing was conducted using Microsoft Excel (Microsoft®, USA). The statistical software GraphPad Prism 5 was used. Normal distribution was determined using a Shapiro-Wilk normality test. Parametric significance was determined using a one-way analysis of variance (ANOVA) and a Bonferroni's multiple comparison test, except section 2.8 where unpaired t-tests were conducted, $p \leqslant 0.05$.

3. Results and discussion

Hyperinflammation and EMT of residual LECs within the capsular bag post-cataract surgery contributes to the development of PCO, a common complication arising from IOL implantation. This study aimed to investigate the impact of $Ti_3C_2T_x$ on LEC intracellular mechanisms leading to an excessive inflammatory response and myofibroblast formation towards PCO development. It was found that $Ti_3C_2T_x$ coatings significantly repressed IL-1β gene and protein expression in IL-1β-primed LECs. A weakened response in the expression of IL-6 and the CXC chemokine subfamily was found when cells were treated with $Ti_3C_2T_x$ and IL-1β relative to cells treated with IL-1β alone suggesting repression of markers linked to the chemokine mediated innate immune response post cataract surgery [18]. $Ti_3C_2T_x$ coatings did not significantly upregulate any hallmark inflammation pathways and LECs showed no significant changes in lipid membrane composition after 24 h incubation with $Ti_3C_2T_x$ coatings. Finally, it was shown that $Ti_3C_2T_x$ coatings promoted a positive resolution of the wound-healing response, by repressing vimentin overexpression and preventing the activation of chronic wound healing response pathways.

3.1. Synthesis and characterisation of $Ti_3C_2T_x$ MXene

$Ti_3C_2T_x$ was etched using *in situ* hydrofluoric acid to selectively remove the aluminium layers in the MAX phase composite Ti_3AlC_2. The solvated lithium ions and subsequent sonication step during processing of $Ti_3C_2T_x$ resulted in a stable delaminated colloidal solution. DLS and SEM analysis was used to quantify flake size and polydispersity index (PDI) of the $Ti_3C_2T_x$ colloidal solutions. DLS showed an average flake size of 471.90 ± 10.97 d.nm and an average PDI of 0.24 ± 0.02 (figure S1(A)). SEM showed the presence of flakes of ∼400 d.nm (figure S2). A PDI of less than 0.5 gives confidence of a monodisperse solution [39], identifying the method was appropriate for size estimations of the solution. Sonication

can increase the likelihood of flake defects [40]. However, for the purpose of the biological evaluation, uniformity in size throughout the colloidal solution was prioritised. Solution concentration was determined by calculating the mass of free-standing films achieved by vacuum filtration. UV–vis spectroscopy can be used to confirm the synthesis of a specific type of MXene. UV–vis spectroscopy produced a broad peak between 700 and 800 nm, attributed to the plasmonic peak of $Ti_3C_2T_x$ synthesis (figure S1(B)) [41]. Contact angle analysis measures the wettability of a material by the contact angle of a water droplet upon touching the external surface of a material [42]. Spin coating hydrophobic IOLs with $Ti_3C_2T_x$ reduced the internal contact angle of the lens from 71.9° ± 10° to 54.1° ± 9.9° indicating that the $Ti_3C_2T_x$ coating increases the wettability of the lens surface, increasing hydrophilicity. The results confirm changes in the wettability of the IOL surface following coating with $Ti_3C_2T_x$ and the hydrophilicity of $Ti_3C_2T_x$ coatings reported in the literature (table S2) [43]. $Ti_3C_2T_x$ coatings used in the experimental conditions were characterised by thickness and stability in culture media using SEM and UV–vis spectroscopy. The coatings had an average thickness of 1–2 μM (figure S3). $Ti_3C_2T_x$ coatings showed good stability in culture media and when analysed with UV–vis spectroscopy the characteristic $Ti_3C_2T_x$ plasmonic peak was absent indicating no degradation into the media after the 24 h incubation (figure S4).

3.2. $Ti_3C_2T_x$-treated cells do not upregulate pro-inflammatory cytokine expression

The chronic wound-healing response of LECs post-cataract surgery has been established as an early progenitor pathway in PCO development [18]. $Ti_3C_2T_x$ was investigated for its ability to incite or repress cytokine production and either induce LECs inflammation potentially contributing to or downregulating the likelihood of PCO. Coatings of 2–5 mg ml^{-1} $Ti_3C_2T_x$ were investigated in the study. This concentration range was previously optimised by Ward *et al* [5], to maintain the conductivity of $Ti_3C_2T_x$ in the AIOL design whilst not compromising transparency. IL-1β has been linked to ocular inflammation as an instigator of chronic inflammation pathways hence this cytokine was both detected for and used to prime LECs to incite an inflammatory response [44]. Additionally, IL-6 has been shown to promote key developmental pathways of PCO by supporting TGF-β2 activation of LECs transdifferentiation pathways and was therefore measured with regard to EMT tendency [19, 20]. Previously, $Ti_3C_2T_x$ has been shown to repress a cytokine response in the acute monocytic leukemia (THP) -1 monocytes [5, 12]. It was hypothesised that $Ti_3C_2T_x$ may act to repress LEC intracellular pathways which normally lead to upregulation of cytokine production contributing to PCO development; a favourable property for a therapeutic approach towards preventing PCO formation.

$Ti_3C_2T_x$ showed, as a colloidal solution and as a transparent coating, the capacity to significantly suppress cytokine production in IL-1β primed cells. After 1 h incubation with $Ti_3C_2T_x$ solution, there was a significant suppression of IL-6 and IL-8 expression ($p \leqslant 0.001$) (figure S5). A significant reduction in IL-1β expression was found when primed cells were exposed to $Ti_3C_2T_x$ coatings compared to cells treated with IL-1β alone ($p \leqslant 0.05$) (figure 1(B)). A marked but not significant reduction in IL-6 was also noted (figure 1(A)). The relationship between IL-6 and IL-1β reduction by $Ti_3C_2T_x$ coatings was further supported by q-PCR analysis and RNA sequencing (figures 1(D) and (E)) (figure S6). IL-1β gene fold expression was significantly reduced in cells treated with $Ti_3C_2T_x$ and IL-1β relative to cells treated with IL-1β alone ($p \leqslant 0.05$) (figure 1(E)). A similar distinct yet not significant reduction was observed in the IL-6 gene fold expression of cells treated with $Ti_3C_2T_x$ and IL-1β. The lack of significance may be due to the concentration of $Ti_3C_2T_x$ that the cells were exposed to. This is supported by Ozulumba *et al* [12], who showed suppression of IL-8 with delaminated $Ti_3C_2T_x$ in colloidal suspension at a concentration of $\geqslant$5 mg ml^{-1}, IL-6 with $\geqslant$10 mg ml^{-1} and tumour necrosis factor (TNF)-α with $\geqslant$50 mg ml^{-1}. Results confirm the role of IL-1β as an instigator of LEC inflammatory response and the potential therapeutic role of $Ti_3C_2T_x$ in repression of these pathways to reduce tendency to PCO.

$Ti_3C_2T_x$ did not upregulate CXCL1 expression although no significant suppression was found (figure 1(C)). This was confirmed by RNA-sequencing (figure S6). CXCL1 is an innate immune response gene known to be a chemokine recruiter for monocytes therefore, this suggests $Ti_3C_2T_x$ may not induce the expression of chemokines to promote monocyte migration. These results demonstrate $Ti_3C_2T_x$ does not incite a cytokine-based inflammatory response in human LECs, could potentially repress the onset of inflammation by suppressing IL-1β expression and suggests that at optimum concentrations, $Ti_3C_2T_x$ may repress IL-1β, IL-6 and CXCL1 expression to limit LEC inflammatory response linked to EMT and PCO.

3.3. Analysis of differentially expressed genes (DEGs) in $Ti_3C_2T_x$-treated cells

During the wound-healing response of LECs, a plethora of cascade pathways are initiated culminating in chronic inflammation and myofibroblast transdifferentiation inducing an altered, fibrotic phenotype. The initial suppression of cytokine production in lens cells treated with $Ti_3C_2T_x$ was explored further by RNA sequencing to potentially elicit any underlying mechanisms linked to anti-inflammatory effect. An unbiased analysis was undertaken to determine

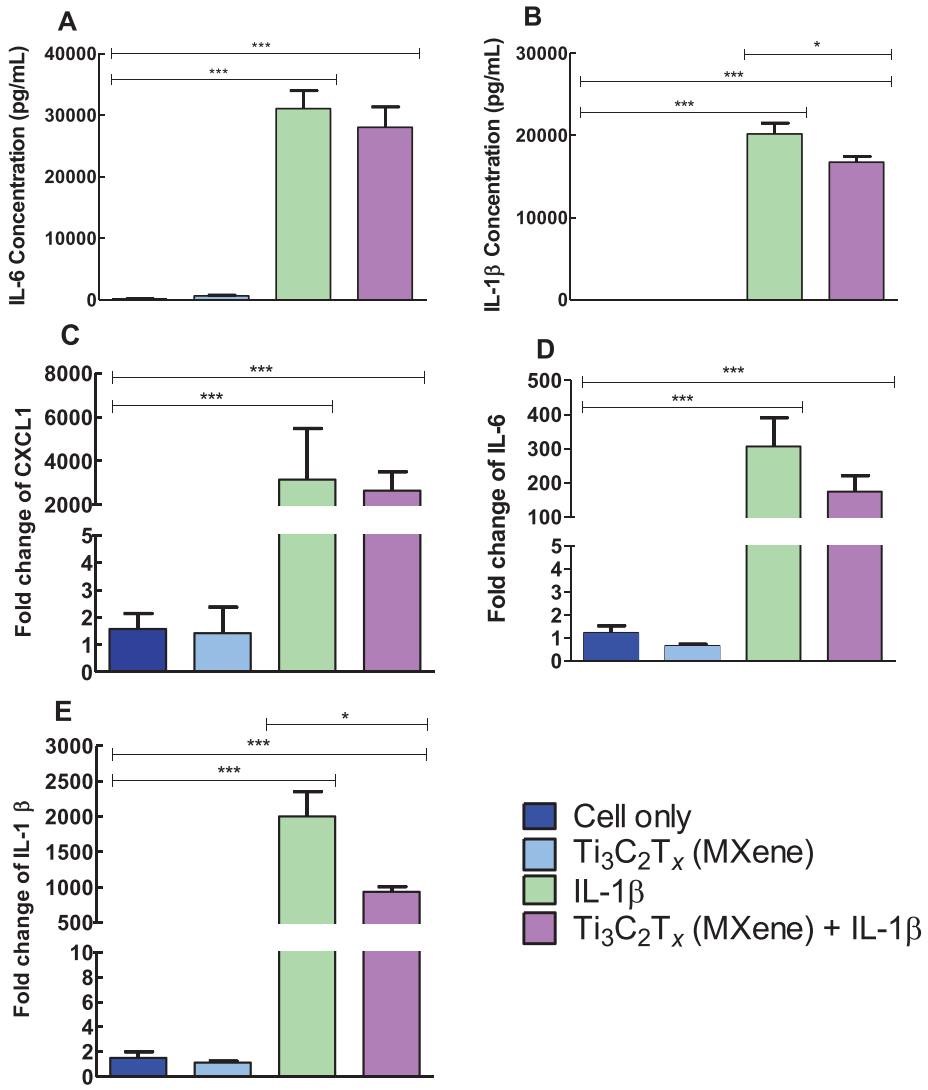

Figure 1. Expression of IL-1β, IL-6 and chemokine CXCL1 by HLE-B3 cells grown on 5 mg ml^{-1} $Ti_3C_2T_x$ coatings. Expression of IL-6 (figure (A)) and IL-1β (figure (B)) was quantified by ELISA. Fold change of *CXCL1* (figure (C)), IL-6 (figure (D)) and IL-1β (figure (E)) gene expression was quantified by q-PCR analysis. IL-1β was used to prime the cells to induce an inflammatory response as a positive inflammation control and as a treatment with $Ti_3C_2T_x$ to elicit any suppression of cytokine expression by $Ti_3C_2T_x$. Media background values were subtracted from all conditions. Cells treated with $Ti_3C_2T_x$ and IL-1β showed a significant reduction in IL-1β ($p \leqslant 0.05$) compared to cells treated with IL-1β alone. Significance was determined using a one-way ANOVA and post-hoc Bonferroni's multiple comparison test for figures (A) and (B) and unpaired two-tailed t tests and F-tests for comparison of variance was used for figures (C)–(E). Significance between the other conditions is denoted with a capped line and asterisks between the groups. $^{*}p \leqslant 0.05$, $^{***}p \leqslant 0.001$. (Cell only: cells alone; $Ti_3C_2T_x$ (MXene): cells grown on $Ti_3C_2T_x$ coatings; IL-1β: cells treated with IL-1β; $Ti_3C_2T_x$ (MXene) + IL-1β: cells grown on $Ti_3C_2T_x$ coatings treated with IL-1β) (Mean $\pm$ SEM; $n = 3$ for figures (A) and (B); $n = 5$ for figure (C)–(E).

which pathways had been altered by the treatment of $Ti_3C_2T_x$ and IL-1β. However, a targeted look at hallmark inflammation gene sets was also completed.

A total of 948 up-regulated DEGs and 896 down-regulated DEGs were identified in LECs treated with IL-1β in comparison to LECs alone. IL-1β significantly upregulated cytokine-cytokine receptor interaction subfamilies CC, CXC, IL6/12-like and IL1 like cytokine, broadly similar to LECs from a mouse cataract surgery model (figure S7(A)) [18]. Despite the limitations in comparisons across species, there were key similarities across the CXC subfamily, a family of chemokines including CXCL1, whose genetic expression was shown to be upregulated in IL-1β primed LECs with some marked reduction following incubation with $Ti_3C_2T_x$ (figure S7(B)). Functional analysis of DEGs performed using clusterProfiler identified several major gene pathways significantly altered by IL-1β treatment (figure S8). These pathways include protein biosynthesis, immune response activation, endoplasmic reticulum stress response, interleukin signalling and ECM re-organisation. This supports the use of IL-1β as a positive control to mimic in part *in vitro* inflammation-primed LECs following post-cataract surgery.

Cells treated with $Ti_3C_2T_x$ had 8 upregulated DEGs and 0 down-regulated DEGs. Of these DEGs, none have been linked to the wound-healing response

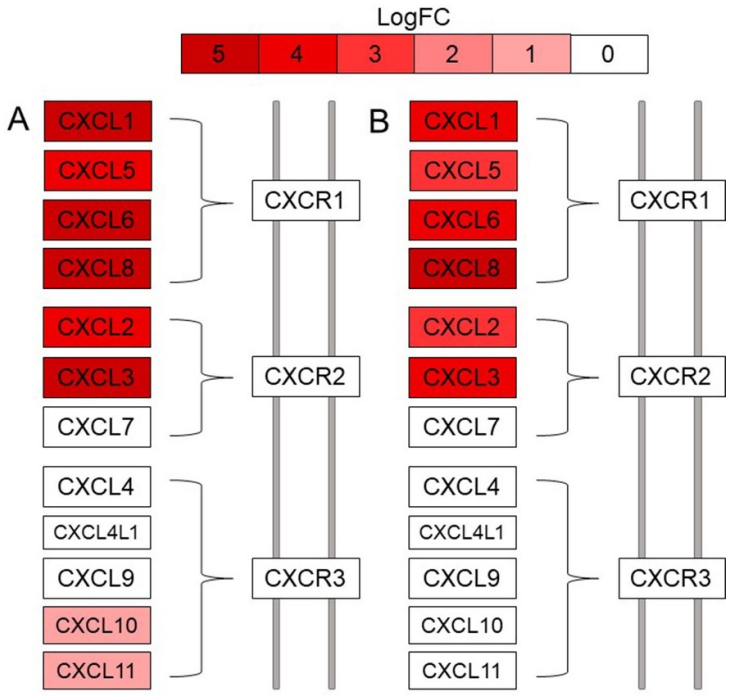

Figure 2. Gene fold change in CXC subfamily of chemokines in FHL124 cells treated with IL-1β (figure (A)) and FHL124 cells treated with $Ti_3C_2T_x$ and IL-1β (figure (B)) involved in cytokine-cytokine receptor interaction, as defined by Kyoto Encyclopaedia of Genes and Genomes [45]. Log fold change represented by colour key. CXCL1-3, 5, 6, 8 and 10 showed a reduction in fold change when cells were treated with $Ti_3C_2T_x$ and IL-1β in comparison to cells treated with IL-1β alone. The full annotated subfamilies are reported in figure S5.

or EMT of LECs. $Ti_3C_2T_x$ did not significantly upregulate any genes involved in the hallmark inflammation pathways in comparison to the cell control (figures S9(A) and (B)). GSEA of hallmark inflammation genes identified a coordinated upregulation in cells treated with IL-1β and down-regulation in cells treated with $Ti_3C_2T_x$. A similar response was found in cells treated with IL-1β and $Ti_3C_2T_x$ comparatively to cells treated with IL-1β alone although several key genes important in the hallmark inflammatory response were more weakly induced including CXCL10, IL-1α and IL-1β (figure S9(C)). Moreover, in the cytokine-cytokine receptor interaction as defined in Kyoto Encyclopaedia of Genes and Genomes [45], a weakened upregulation can also be seen in the innate chemokine subfamily, CXC (figure 2) (figure S7(B)). This suggests there is a weakened upregulation of chemokines when cells are treated with $Ti_3C_2T_x$ and IL-1β relative to cells treated with IL-1β alone.

3.4. Lipid profile of IL-1β-primed and $Ti_3C_2T_x$-treated cells

It is well established that the lipid composition of cells is sensitive to the chemical composition of the growth environment, oxidative stress and nutrients [46] and the physical properties of lipids impact membrane function [47]. Previous work has shown that ocular irritants, such as detergents and other chemicals used in the treatment of eye disorders cause significant alterations in the lipid composition of human corneal epithelial cells [48]. Several studies suggest that MXene nanosheets are cell penetrating 'nano thermal blades' [49], entering cells by partitioning through the plasma membrane, where they exert an antibacterial effect [50]. Since $Ti_3C_2T_x$ would be applied to surfaces intended for use in the ocular environment, the lipidomic profile of LECs was determined to assess biocompatibility in this context. Cells were grown in the presence and absence of $Ti_3C_2T_x$, in addition to the pro-inflammatory stimulant IL-1β. Figure 3 shows the total quantified lipid composition the major lipid classes found in FHL124 cells. Figures S10–S21 show the fatty acid distribution of the individual lipid classes.

The lipidomic analysis in figure 3 quantified 12 different lipid classes. Phosphatidylcholine (PC) lipids were the most dominant lipid, such that PC and plasmenyl-PC lipid were collectively *circa* 60% of total quantified lipid. Phosphatidylethanolamine lipids (PE and plasmenyl-PE lipids) were the second most abundant at 20% of the total quantified lipid. These values agree with the lipidome of LECs cells reported [51] where PC and PE are roughly 50% and 20%, respectively. No statistically significant changes in the total amount of individual lipid classes of LECs cells were observed in the presence of $Ti_3C_2T_x$. This evidence suggests that $Ti_3C_2T_x$ does not behave like other ocular irritants and has good biocompatibility in the ocular environment, at the concentrations

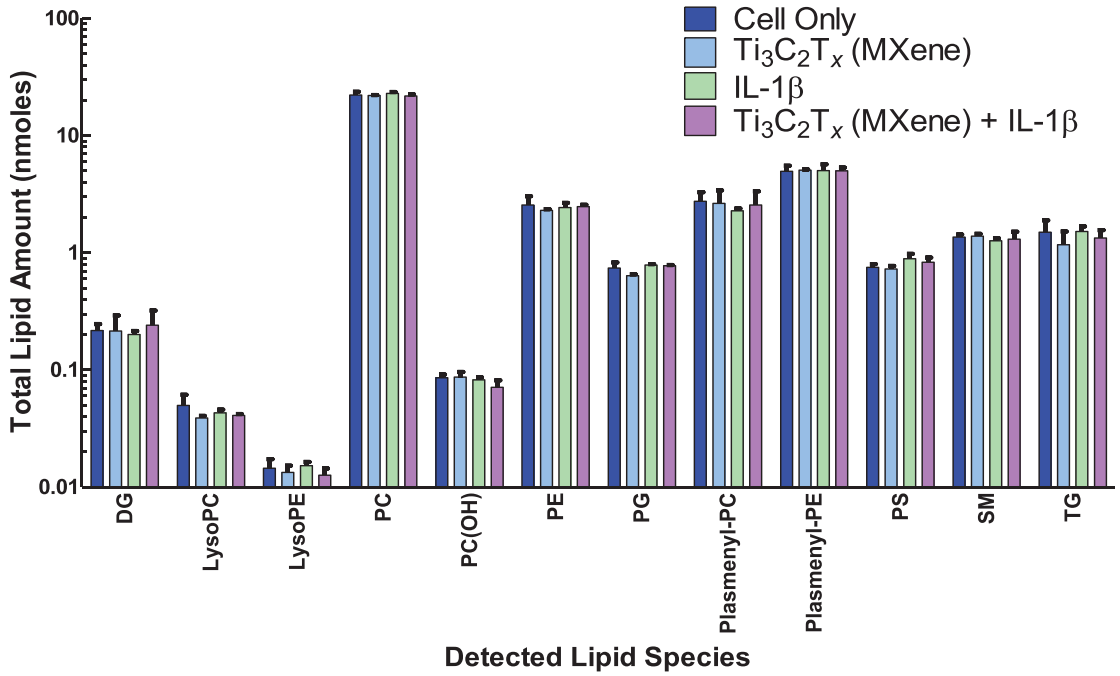

Figure 3. Detected lipid classes in FHL124 cells exposed to pro-inflammatory stimulus, IL-1β and MXene. Individual lipid classes identified were diacyl glycerides (DG), lysophosphatidylcholines (LysoPC), lysophosphatidylcholines (LysoPE), phosphatidylcholines (PC), hydroxy phosphatidylcholines (PC(OH)), phosphatidylethanolamines (PE), phosphatidylglycerols (PG), plasmenyl phosphatidylcholines (Plasmenyl-PC), plasmenyl phosphatidylethanolamines (Plasmenyl-PE), phosphatidylserines (PS), sphingomyelins (SM) and triacylglycerols (TG). (Cell only: cells alone; $Ti_3C_2T_x$ (MXene): cells grown on $Ti_3C_2T_x$ coatings; IL-1β: cells treated with IL-1β; $Ti_3C_2T_x$ (MXene) + IL-1β: cells grown on $Ti_3C_2T_x$ coatings treated with IL-1β) (Mean $\pm$ SD; $n = 3$).

studied. Incubation in the presence of IL-1β can cause increases in diacylglycerol (DG) lipids [52] but these are typically transient occurring within a few minutes of initiation. IL-1β did not cause significant changes in the total lipid profile at 24 h (figure 3). Figures S10–21 show the fatty acid compositional profile of the lipid classes studied, in order of highest compositional abundance. Lipids containing saturated and monounsaturated fatty acids such as palmitic acid (16:0), stearic (18:0) and oleic acid (18:1) were the most abundant in each of the different lipid classes observed. This is normal for mammalian cell lines [53]. In general, only small compositional changes in the fatty acid profile of the individual lipid classes were observed, which are probably not significant. Exceptions to this were phosphatidylglycerols (PG) lipids, which were compositionally richer in PG 16:0_18:1 (figure S16) and DG lipids, that were compositionally reduced in DG 16:0_18:1 and DG 18:1_18:1 (figure S10) when incubated with IL-1β alone and $Ti_3C_2T_x$ with IL-1β. Similarly, Lyso PC (LPC) lipids were richer in LPC 16:0 but reduced in LPC 18:0 in the presence of IL-1β alone and $Ti_3C_2T_x$ with IL-1β (figure S11) and PC lipids were richer in PC 32:0 (probably PC 16:0_16:0) in the presence of $Ti_3C_2T_x$ with IL-1β. Finally sphingomyelins (SM) was compositionally richer in SM 34:0 (possibly SM 18:0_16:0) in the presence of IL-1β and $Ti_3C_2T_x$ with IL-1β alone and reduced in SM 42:3 in the presence of IL-1β. Lipids like SM, PC, LPC, DG and PG are lipid messengers involved in mediating inflammation and wound healing in other non-ocular cell lines [54, 55]. The changes seen in these lipids in IL-1β and $Ti_3C_2T_x$ and IL-1β alone samples may reflect an inflammatory response in a small subset of saturated/monounsaturated lipids containing 16:0 and 18:1 fatty acids, further work will be required to elucidate the significance of this.

3.5. $Ti_3C_2T_x$ does not promote the expression of key EMT markers in lens cells

The EMT of LECs post-cataract surgery is the subsequent stage contributing to the cells' ability to migrate across the IOL and posterior capsule optic range, obscuring vision. The presence of $Ti_3C_2T_x$ coatings on cell migration was observed using scratch assay analysis. $Ti_3C_2T_x$ promoted LECs migration, showing a significantly increased rate of wound closure after 48 h in comparison to a non-coated tissue-culture graded well ($p < 0.01$) (figure 4). This may be as a result of the hydrophilic nature of $Ti_3C_2T_x$, confirmed by contact angle analysis (table S2) increasing surface wettability that provides a favourable surface for an improved scratch/wound closure response [56]. The repression of inflammation markers with positive healing processes by $Ti_3C_2T_x$ suggests itself

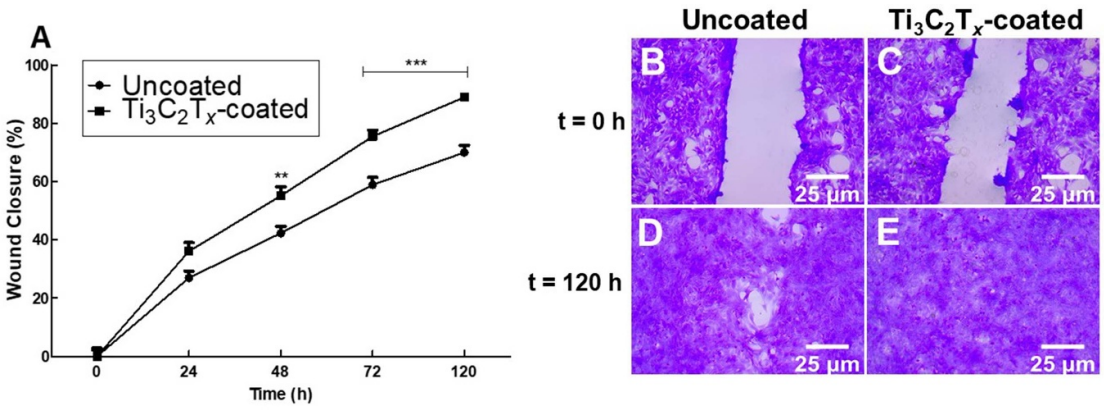

Figure 4. Human lens epithelial (HLE-B3) cells grown on uncoated and $Ti_3C_2T_x$-coated tissue grade 12-well plates. Wound closure rate was quantified using light microscope images taken at the selected time points (figure (A)). Light microscope images of HLE-B3 cells grown on uncoated (figures (B) and (D)) and $Ti_3C_2T_x$-coated (figures (C) and (E)) stained with crystal violet at $t = 0$ h (top) and $t = 120$ h (bottom). $x50$ magnification by light microscope (Zeiss Primovert HDcam, Germany). Scale bar: 25 μM. Measurements were calculated using Fiji Image J. Wound closure was calculated as the width difference in the scratch across the cell monolayer at $t = 0$ h relative to the other time points. A two-way ANOVA was completed using GraphPad Prism 5. $^{**}p < 0.01$; $^{***}p < 0.001$. (Uncoated: cells grown on tissue culture well; $Ti_3C_2T_x$-coated: cells grown on $Ti_3C_2T_x$-coated wells) (Mean ± SEM; $n = 6$).

as a potentially biocompatible material on exposure to LECs with the capacity to stimulate wound closure and wound healing following AIOL device implantation.

Post-cataract surgery, latent TGF-β2 is activated by migrating macrophages, attracted by the elevated cytokine production of LECs undergoing a wound-healing response. TGF-β drives EMT of LECs, transforming the epithelial cells into myofibroblasts, recognised by their elongated nuclei and branched-like ECM [57]. During myofibroblast formation, TGF-β initiates a cascade of signalling pathways, of which the SMAD2/3 pathway is most recognised [58]. SMAD-signalling upregulates TGF-β gene transcription, activates Rho GTPases and stimulates the PI3/Akt, MAPK pathways. These events are associated with EMT-related matrix contraction, cell differentiation and inhibition of cell proliferation [13].

To investigate the impact of $Ti_3C_2T_x$ on the EMT pathway, the FHL124 cell line was used as these cells respond similarly to *in vivo* LECs with regard to EMT characteristics [16]. SMAD2/3 was investigated to quantify differentiation of LECs. α-SMA is expressed in normal state LECs in various species [59]. Myofibroblasts have an accumulation of α-SMA due to the upregulation of TGF-β signalling which is used to qualitatively measure cell differentiation and migration [57]. Vimentin plays a central role in the wound healing response of the lens epithelium post-cataract surgery [60]. In mock surgeries, the epithelium repair cells which function in the migration of residual LECs over the wounded area have high expression of vimentin filaments [60]. Therefore, vimentin was also investigated as a marker for mesenchymal differentiation and cell migration [61]. These markers were quantified using immunocytochemistry and western blot analysis.

FHL124 cells without treatment showed limited fluorescence for all three markers (figures 5(A), (E) and (I)). $Ti_3C_2T_x$ treatment alone did not upregulate EMT marker expression indicating no tendency to promote EMT (figures 5(B), (F) and (J)). TGF-β2 was used to prime the LECs to undergo myofibroblast differentiation. Cells exposed to TGF-β2 showed morphological changes, changing from rounded clusters of cells to elongated branch-like structures (figures 5(C) and (G)). Intensity of α-SMA, SMAD2/3 and vimentin staining were increased in cells treated with TGF-β2 (figures 5(C), (G) and (K)). Following quantification of antibody staining using ImageJ, a significant reduction in vimentin expression was found ($p \leqslant 0.01$) (figure 5(N)) and a marked but not statistically significant reduction in α-SMA and SMAD2/3 expression was found in cells treated with $Ti_3C_2T_x$ and TGF-β2 compared to the TGF-β2 stimulated control (figures 5(M) and (O)). No significant difference in cell number was found between control and treated conditions as quantified by DAPI stain (figure S22).

The immunocytochemistry results were supported by the western blots analysis. α-SMA, vimentin and SMAD2/3 expression were significantly upregulated in cells treated with TGF-β2 compared to the cell only control ($p \leqslant 0.05$). $Ti_3C_2T_x$ did not significantly alter but did markedly reduce α-SMA and SMAD2/3 expression in cells treated without and with TGF-β2 in comparison to the cell only and TGF-β2-primed cells respectively (figures 6(A) and (C)). Detection of vimentin was significantly downregulated in cells treated with TGF-β2 and $Ti_3C_2T_x$, supporting

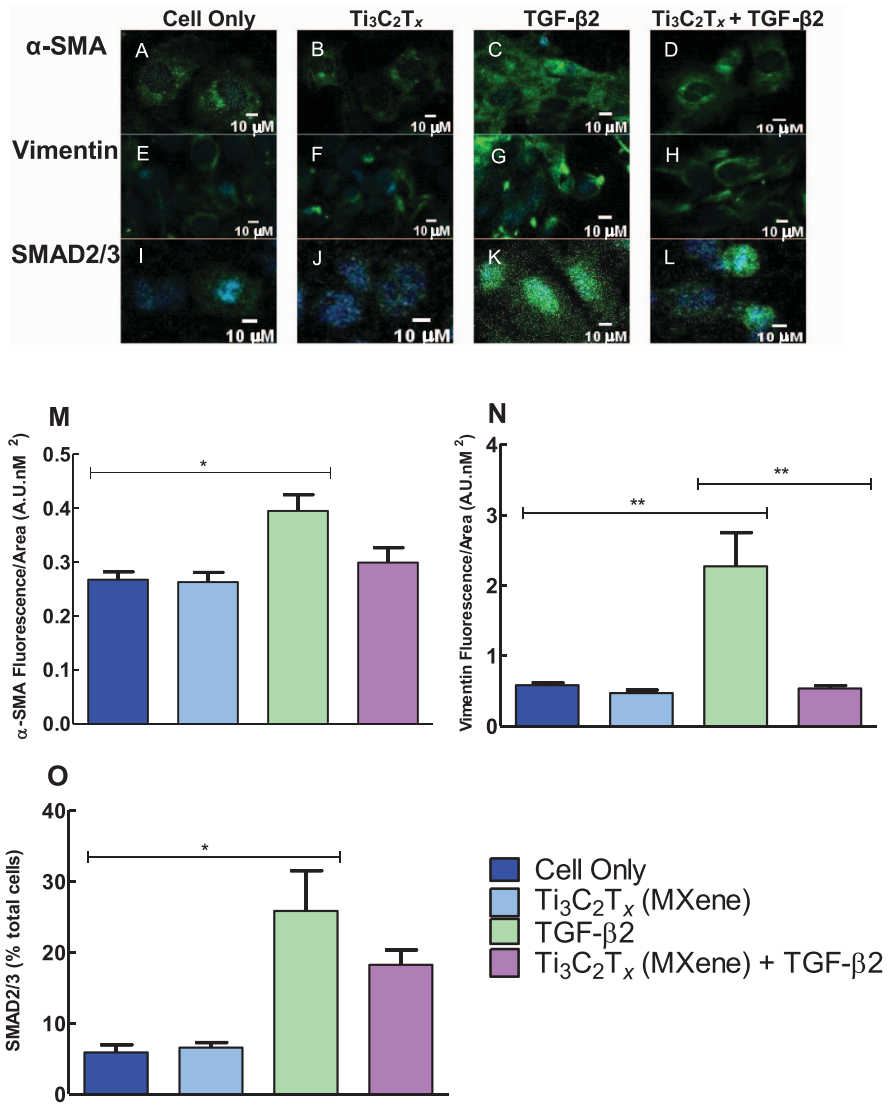

Figure 5. Alpha smooth muscle (α-SMA), vimentin and SMAD2/3 stain of FHL124 cells treated with 2 mg ml^{-1} $Ti_3C_2T_x$ and TGF-β2 quantified by immunocytochemistry. Expression of α-SMA by cell only (figure (A)), cells with $Ti_3C_2T_x$ (figure (B)), cells with TGF-β2 (figure (C)) and cells with TGF-β2 and $Ti_3C_2T_x$ (figure (D)). Expression of vimentin by cell only (figure (E)), cells with $Ti_3C_2T_x$ (figure (F)), cells with TGF-β2 (figure (G)) and cells with TGF-β2 and $Ti_3C_2T_x$ (figure (H)). Expression of SMAD2/3 by cells only (figure (I)), cells with $Ti_3C_2T_x$ (figure (J)), cells with TGF-β2 (figure (K)) and cells with TGF-β2 and $Ti_3C_2T_x$ (figure (L)). Images were quantified using Fiji:Image J by the fluorescence of each protein across the area of the cell sample for α-SMA (figure (M)) and vimentin (figure (N)). SMAD2/3 nuclei stain was normalised across the conditions against the DAPI cell count (figure (O)). Non-specific binding of the secondary antibody was subtracted from the fluorescence intensity of the cell only and treated conditions for α-SMA and SMAD2/3 quantification. An excitation filter of 488 nm was used. Cells were primed with TGF-β2 as a positive control for mesenchymal differentiation. A significant downregulation of vimentin expression was found in cells treated with $Ti_3C_2T_x$ and TGF-β2 relative to cells treated with TGF-β2 alone ($p \geqslant 0.05$). A one-way ANOVA and Bonferroni's multiple comparison test was completed using GraphPad Prism 5. Significance between the cell only (Cell only) and the other conditions are denoted by asterisks directly above the columns. Significance between the other conditions is denoted with a capped line and asterisks between the groups. $^{*}p \geqslant 0.05$, $^{**}p \geqslant 0.01$. (Cell only: cells alone; $Ti_3C_2T_x$ (MXene): cells grown on $Ti_3C_2T_x$ coatings; TGF-β2: cells treated with TGF-β2; $Ti_3C_2T_x$ (MXene) + TGF-β2: cells grown on $Ti_3C_2T_x$ coatings treated with TGF-β2) (Mean $\pm$ SEM; $n = 3$.)

the immunocytochemistry quantification shown in figure 5(N) (figure 6(B)). Raw densitometry data is shown in table S3. This study has shown cell migration rate is significantly increased when cells are grown over $Ti_3C_2T_x$ coatings (figure 4(A)). Conversely, vimentin is a protein filament that is highly expressed during cell migration which was shown in this study to be significantly downregulated in cells treated with $Ti_3C_2T_x$ and TGF-β2 [60, 61]. This could be as a result of $Ti_3C_2T_x$ promoting a positive resolution of the wound healing response in cells by suppressing vimentin expression to prevent overexpression and chronic wound response pathways. These results suggest $Ti_3C_2T_x$ may not upregulate cell differentiation and myofibroblast formation and promote good resolution of the wound closure response in LECs if incorporated in an AIOL device.

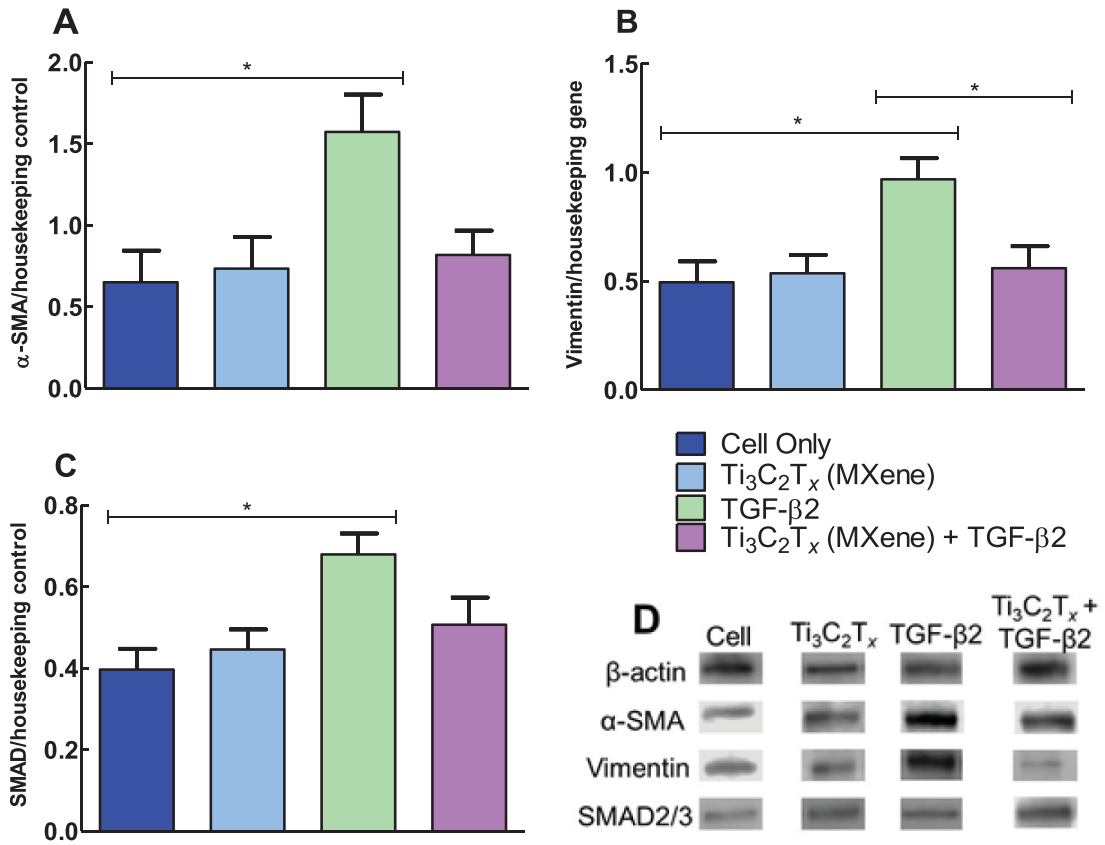

Figure 6. Western blot analysis for the expression of α-SMA, vimentin and SMAD in FHL124 cells treated with 2 mg ml^{-1} $Ti_3C_2T_x$. Net protein expression of α-SMA (figure (A)), vimentin (figure (B)) and SMAD (figure (C)). was normalised and quantified as ratio to its beta-actin (β-actin) expression. Images of the visualised protein bands (20 μG) in each of the control and treatment groups against their beta-actin (β-actin) expression (figure (D)). TGF-β2 was used as a positive control for epithelial-mesenchymal transition. A significant upregulation in cells treated with TGF-β2 was found ($p \leqslant 0.05$) in comparison to the other condition. A significant downregulation in vimentin expression was observed in cells treated with $Ti_3C_2T_x$ and TGF-β2 relative to cells treated with TGF-β2 only ($p \leqslant 0.05$). A one-way ANOVA and Bonferroni's multiple comparison test was conducted using GraphPad Prism 5. Significance between the cell only (Cell only) and the other conditions are denoted by asterisks directly above the columns. Significance between the other conditions is denoted with a capped line and asterisks between the groups. $^*p \geqslant 0.05$. (Cell only: cells alone; $Ti_3C_2T_x$ (MXene): cells grown on $Ti_3C_2T_x$ coatings; TGF-β2: cells treated with TGF-β2; $Ti_3C_2T_x$ (MXene) + TGF-β2: cells grown on $Ti_3C_2T_x$ coatings treated with TGF-β2) (Mean $\pm$ SEM; $n = 5$.)

4. Conclusions

In summary, $Ti_3C_2T_x$ MXene acted to repress release of pro-inflammatory cytokine IL-1β and promoted a positive resolution of the wound response, with a marked downregulation of key myofibroblast differentiation markers. A mechanism linked to the repression of the cytokine-cytokine receptor interactions by $Ti_3C_2T_x$ is suggested. Further work to optimise the positive interaction of $Ti_3C_2T_x$ within the AIOLs device for more significant repression of LECs propensity towards PCO, potentially through drug elution mechanisms, could be used to provide cataract patients with a preventative treatment against posterior capsule opacification development.

Data availability statement

All data that support the findings of this study are included within the article (and any supplementary files).

Acknowledgment

This work was supported by University of Brighton Scholarship with the Doctoral Training Alliance Bioscience Programme (G2059). The authors would like to acknowledge the Centre for Regenerative Medicine and Devices (G2434) and Centre for Stress and Age-Related Diseases (G2435) for providing the funding for the genomics analysis and the University of Brighton Genomics Facility for completing this analysis. The authors would like to thank Mohamed Alhabeb and Tyler Mathis for providing MAX phase and performing SEM characterisation at the Core Research Facilities (CRF) at Drexel University. The authors would like to thank Jon Salvage at the School of Applied Sciences at University of Brighton for performing additional SEM analysis. The authors would also like to thank Emma Ward for their valuable contribution.

Conflict of interest

The authors declare no conflict of interest.

ORCID iDs

Grace Cooksley https://orcid.org/0000-0001-8186-9442
Marcus K Dymond https://orcid.org/0000-0002-9903-4993
Nicolas A Stewart https://orcid.org/0000-0002-8969-4242
Giselda Bucca https://orcid.org/0000-0001-5286-7771
Andrew Hesketh https://orcid.org/0000-0001-5220-8733
Yury Gogotsi https://orcid.org/0000-0001-9423-4032
Susan Sandeman https://orcid.org/0000-0001-8367-2758

References

[1] Hashemi H, Pakzad R, Yekta A, Aghamirsalim M, Pakbin M, Ramin S and Khabazkhoob M 2020 Global and regional prevalence of age-related cataract: a comprehensive systematic review and meta-analysis *Eye* **34** 1357–70
[2] Allen D and Vasavada A 2006 Cataract and surgery for cataract *Br. Med. J.* **333** 128–32
[3] Bellucci R 2013 An introduction to intraocular lenses: material, optics, haptics, design and aberration *Cataract* **3** 38–55
[4] Alió J L, Del Barrio J L A and Vega-Estrada A 2017 Accommodative intraocular lenses: where are we and where we are going *Eye Vis.* **4** 16
[5] Ward E J *et al* 2020 2D titanium carbide ($Ti_3C_2T_x$) in accommodating intraocular lens design *Adv. Funct. Mater.* **30** 2000841
[6] Naguib M, Kurtoglu M, Presser V, Lu J, Niu J, Heon M, Hultman L, Gogotsi Y and Barsoum M W 2011 Two-dimensional nanocrystals produced by exfoliation of Ti_3AlC_2 *Adv. Mater.* **23** 4248–53
[7] Naguib M, Mochalin V N, Barsoum M W and Gogotsi Y 2014 25th anniversary article: mXenes: a new family of two-dimensional materials *Adv. Mater.* **26** 992–1004
[8] Soleymaniha M, Shahbazi M A, Rafieerad A R, Maleki A and Amiri A 2019 Promoting role of mxene nanosheets in biomedical sciences: therapeutic and biosensing innovations *Adv. Healthcare Mater.* **8** 1
[9] Lin H, Chen Y and Shi J 2018 Insights into 2D MXenes for versatile biomedical applications: current advances and challenges ahead *Adv. Sci.* **5** 1800518
[10] Han X, Huang J, Lin H, Wang Z, Li P and Chen Y 2018 2D ultrathin MXene-based drug-delivery nanoplatform for synergistic photothermal ablation and chemotherapy of cancer *Adv. Healthcare Mater.* **7** 1701394
[11] Yin S *et al* 2022 MXene-contact enhanced broadband photodetection in centimeter level GeS films *J. Appl. Phys.* **55** 265105
[12] Ozulumba T, Ingalve G, Gogotsi Y and Sandeman S 2021 Moderating cellular inflammation using 2-dimensional titanium carbide MXene and graphene variants *Biomater. Sci.* **9** 1805–15
[13] Nibourg M L, Gelens E, Kuijwe R, Hooymans J M M, van Kooten G T and Koopmans A S 2015 Prevention of posterior capsular opacification *Exp. Eye Res.* **136** 100–15
[14] Raj S M, Vasavada A R, Johar S K, Vasavadam V A and Vasavada V A 2007 Post-operative capsular opacification: a review *Int. J. Biomed. Sci.* **3** 237–50
[15] Awasthi N, Wang-Su S T and Wagner B J 2008 Downregulation of MMP-2 and −9 by proteasome inhibition: a possible mechanism to decrease LEC migration and prevent posterior capsular opacification *Invest. Ophthalmol. Vis. Sci.* **49** 5
[16] Wormstone I M, Wang L and Liu C S C 2009 Posterior capsule opacification *Exp. Eye Res.* **88** 257–69
[17] Cooksley G, Dymond M K, Lacey J and Sandeman S 2021 Factors affecting posterior capsule opacification in the development of intraocular lens materials *Pharmaceutics* **13** 860
[18] Jiang J, Shihan M H, Wang Y and Duncan M K 2018 Lens epithelial cells initiate an inflammatory response following cataract surgery *Invest. Ophthalmol. Vis. Sci.* **59** 4986–97
[19] Ma B, Yang L, Jing R, Liu J, Quan Y, Hui Q, Li J, Qin L and Pei C 2018 Effects of Interleukin-6 on posterior capsular opacification *Exp. Eye Res.* **172** 94–103
[20] Lewis A C 2013 Interleukin-6 in the pathogenesis of posterior capsule opacification and the potential role for interleukin-6 inhibition in the future of cataract surgery *Med. Hypotheses* **80** 466–74
[21] Sinha R, Shekhar H, Sharma N, Titiyal J S and Vajpayee R B 2013 Posterior capsular opacification: a review *Indian J. Ophthalmol.* **61** 371–6
[22] Wertheimer C *et al* 2017 The intraocular lens as a drug delivery device: *in vitro* screening of pharmacologic substances for the prophylaxis of posterior capsule opacification *Investig. Ophthalmol. Vis. Sci.* **58** 6408–18
[23] Smith A, J O, Eldred J A and Wormstone I M 2019 Resveratrol inhibits wound healing and lens fibrosis: a putative candidate for posterior capsule opacification prevention *Investig. Ophthalmol. Vis. Sci.* **60** 3863–77
[24] Liu D *et al* 2022 Nanoporous gold ring-integrated photothermal intraocular lens for active prevention of posterior capsular opacification *Small* **18** 2201098
[25] Zhu Y, Sui B, Liu X and Sun J 2021 The reversal of drug resistance by two-dimensional titanium carbide Ti_2C (2D Ti_2C) in non-small-cell lung cancer via the depletion of intracellular antioxidant reserves *Thorac. Cancer* **12** 3340–55
[26] Ye Z, Huang Y, Li J, Ma T, Gao L, Huihui H, He Q, Jin H and Li Z 2022 Two-dimensional ultrathin Ti_3C_2 MXene nanosheets coated intraocular lens for synergistic photothermal and NIR-controllable rapamycin releasing therapy against posterior capsule opacification *Front. Bioeng. Biotechnol.* **10** 989099
[27] Wormstone I M, Tamiya S, Eldred J A, Lazaridis K, Chantry A, Reddan J R, Anderson I and Duncan G 2004 Characterisation of TGF-β2 signalling and function in a human lens cell line *Exp. Eye Res.* **78** 705–14
[28] Suarez-Amedo A, Figueroa F T, Clavijo C, Arbeláez P and Cruz J C 2020 An image J plugin for the high throughput image analysis of *in vitro* scratch wound healing assays *PLoS One* **15** e0232565
[29] Shihan M H, Novo S G, Marchand S J L, Wang Y, Duncan M K and Professor F 2021 A simple method for quantitating confocal fluorescent images *Biochem. Biophys. Rep.* **25** 100916
[30] Ewels P, Magnusson M, Lundin S and Käller M 2016 MultiQC: summarize analysis results for multiple tools and samples in a single report *Bioinformatics* **32** 3047–8
[31] Kim D, Paggi J M, Park C, Bennett C and Salzberg S L 2019 MultiQC: summarize analysis results for multiple tools and samples in a single report *Nat. Biotechnol.* **37** 907–15
[32] Patro R, Duggal G, Love M, Irizarry R and Kingsford C 2017 Salmon provides fast and bias-aware quantification of transcript expression *Nat. Methods* **14** 417–9
[33] Love M I, Huber W and Anders S 2014 Moderated estimation of fold change and dispersion for RNA-seq data with DESeq2 *Genome Biol.* **15** 550
[34] Yu G, Wang L-G, Han Y and He Q-Y 2012 clusterProfiler: an r package for comparing biological themes among gene clusters *OMICS* **16** 284–7
[35] Bligh E G and Dyer W J 1959 A rapid method of total lipid extraction and purification *Can. J. Biochem. Physiol.* **37** 911–7

[36] Kessner D, Chambers M, Burke R, Agus D and Mallick P 2008 ProteoWizard: open source software for rapid proteomics tools development *Bioinformatics* **24** 2534–6
[37] Hutchins P D, Russell J D and Coon J J 2018 LipiDex: an integrated software package for high-confidence lipid identification *Cell Syst.* **6** 621–5
[38] Katajamaa M, Miettinen J and Orešič M 2006 MZmine: toolbox for processing and visualization of mass spectrometry based molecular profile data *Bioinformatics* **22** 634–6
[39] Danaei M, Dehghankhold M, Ataei S, Hasanzadeh Davarani F, Javanmard R, Dokhani A, Khorasani S and Mozafari M R 2018 Impact of particle size and polydispersity index on the clinical applications of lipidic nanocarrier systems *Pharmaceutics* **10** 2
[40] Maleski K, Ren C E, Zhao M Q, Anasori B and Gogotsi Y 2018 Size-dependent physical and electrochemical properties of two-dimensional MXene flakes *ACS Appl. Mater. Interfaces* **10** 24491–8
[41] Maleski K, Shuck C E, Fafarman A T and Gogotsi Y 2020 The broad chromatic range of two-dimensional transition metal carbides *Adv. Opt. Mater.* **9** 2001563
[42] Yuan Y and Lee T R 2013 Contact angle and wetting properties *Surface Sciences Techniques* vol 51, ed G Bracco and B Holst (Berlin: Springer) pp 3–34
[43] Anasori B, Lukatskaya M R and Gogotsi Y 2017 2D metal carbides and nitrides (MXenes) for energy storage *Nat. Rev. Mater.* **2** 16098
[44] Dinarello C A 2018 Overview of the IL-1 family in innate inflammation and acquired immunity *Immunol. Rev.* **281** 8–27
[45] Kanehisa M, Furumichi M, Tanabe M, Sato Y and Morishima K 2017 KEGG: new perspectives on genomes, pathways, diseases and drugs *Nucleic Acids Res.* **45** D353–61
[46] Symons J L, Cho K J, Chang J T, Du G, Waxham M N, Hancock J F, Levental I and Levental K R 2021 Lipidomic atlas of mammalian cell membranes reveals hierarchical variation induced by culture conditions, subcellular membranes, and cell lineages *Soft Matter* **17** 288–97
[47] Dymond M K 2021 Lipid monolayer spontaneous curvatures: a collection of published values *Chem. Phys. Lipids* **239** 105117
[48] Magny R *et al* 2020 Lipidomic analysis of human corneal epithelial cells exposed to ocular irritants highlights the role of phospholipid and sphingolipid metabolisms in detergent toxicity mechanisms *Biochimie* **178** 148–57
[49] Wu D, Zhao R, Chen Y, Wang Y, Li J and Fan Y 2021 Molecular insights into MXene destructing the cell membrane as a "nano thermal blade" *Phys. Chem. Chem. Phys.* **23** 3341–50
[50] Rasool K, Helal M, Ali A, Ren C E, Gogotsi Y and Mahmoud K A 2016 Antibacterial activity of $Ti_3C_2T_x$ MXene *ACS Nano* **10** 3674–84
[51] Huang L, Estrada R, Yappert M C and Borchman D 2006 Oxidation-induced changes in human lens epithelial cells: 1 phospholipids *Free Radic. Biol. Med.* **41** 1425–32
[52] Welsh N 1996 Interleukin-1β-induced ceramide and diacylglycerol generation may lead to activation of the c-Jun NH2-terminal kinase and the transcription factor ATF2 in the insulin-producing cell line RINm5F *J. Biol. Chem.* **271** 8307–12
[53] Haider A *et al* 2018 PCYT1A regulates phosphatidylcholine homeostasis from the inner nuclear membrane in response to membrane stored curvature elastic stress *Dev. Cell* **45** 481–95
[54] Knuplez E and Marsche G 2020 An updated review of pro- and anti-inflammatory properties of plasma lysophosphatidylcholines in the vascular system *Int. J. Mol. Sci.* **21** 4501
[55] Tokumura A, Taira S, Kikuchi M, Tsutsumi T, Shimizu Y and Watsky M A 2012 Lysophospholipids and lysophospholipase D in rabbit aqueous humor following corneal injury *Prostaglandins Other Lipid Mediat.* **97** 83–89
[56] Lee J H, Khang G, Lee J W and Lee H B 1998 Interaction of different types of cells on polymer surfaces with wettability gradient *J. Colloid Interface Sci.* **205** 323–30
[57] Joseph R, Bales K, Srivastava K and Srivastava O 2019 Lens epithelial cells-induced pluripotent stem cells as a model to study epithelial-mesenchymal transition during posterior capsular opacification *Biochem. Biophys. Rep.* **20** 100696
[58] Walton K L, Johnson K E and Harrison C A 2017 Targeting TGF-β mediated SMAD signaling for the prevention of fibrosis *Front. Pharmacol.* **8** 461
[59] Garcia C M, Kwon G P and Beebe D C 2006 α-Smooth muscle actin is constitutively expressed in the lens epithelial cells of several species *Exp. Eye Res.* **83** 999–1001
[60] Menko A S, Bleaken B M, Libowitz A A, Zhang L, Stepp M A and Walker J L 2014 A central role for vimentin in regulating repair function during healing of the lens epithelium *Mol. Biol. Cell* **25** 776–90
[61] Usman S, Waseem N H, Nguyen T K N, Mohsin S, Jamal A, Teh M-T and Waseem A 2021 Vimentin is at the heart of epithelial mesenchymal transition (EMT) mediated metastasis *Cancers* **13** 4985